Combustion and Flame 282 (2025) 114465

Contents lists available at ScienceDirect

Combustion and Flame

journal homepage: www.sciencedirect.com/journal/combustion-and-flame

Studies of real-fluid supercritical simulation using the 3rd virial equation of state based on Boltzmann-weighted Full-dimensional potential

Xin Zhang, Junfeng Bai, Hao Zhao *

School of Mechanics and Engineering Science, Peking University, Beijing, 100871, China

ARTICLE INFO

Keywords:
Supercritical combustion
Real-fluid effect
Potential model
Third-order virial equation of state
Cantera

ABSTRACT

Under extreme conditions such as supercritical combustion, real-fluid effects become significant, necessitating accurate and robust simulation methodologies for high-pressure environments. In this study, we propose a real-fluid simulation method, the BWF-Virial method, which integrates the Boltzmann-weighted Full-dimensional (BWF) potential into the virial equation of state (EoS) for physical properties and combustion characteristics simulations under high to ultra-high pressures. Based on the BWF potential model, the second and third virial coefficients, along with their corresponding thermodynamic and transport properties, are rigorously derived. These methods are subsequently integrated into the Cantera software package, establishing a comprehensive real-fluid simulation platform. The BWF-Virial method attains the accuracy of the third-order virial EoS, thereby offering a precise description of real-fluid behavior for various fuels. Its effectiveness has been validated through thermodynamic and transport property calculations across various species, with relative errors of 0.1%–10%. We further investigate zero-dimensional and one-dimensional combustion characteristics of supercritical methane and n-heptane. The BWF-Virial method demonstrates strong robustness and predictive accuracy in modeling combustion phenomena across a wide range of extreme operating conditions. Compared to the LJ-Virial method, it exhibits a 5%–20% difference, aligning more closely with experimental data and reinforcing its potential for high-fidelity supercritical combustion simulations.

Novelty and significance statement

The novelty of this research lies in the development of the BWF-Virial method for real-fluid supercritical simulations. Real-fluid effects are significantly amplified in non-ideal flows, such as supercritical fluids and plasmas. These flows are highly relevant to propulsion and energy conversion processes. Unfortunately, the real-fluid intermolecular interactions in the literature are mainly based on the Lennard-Jones potential, which reveals significant errors for physical properties and combustion simulations at high to ultra-high pressures, especially for polar and long-chain molecules. The BWF-Virial method can effectively overcome these limitations. It provides comprehensive and robust support in (i) the thermodynamic and transport property library establishment for polar and long-chain molecules, (ii) the reactive real-fluid combustion simulations, and (iii) the physical investigations of real-fluid impact on reactive flow simulations.

1. Introduction

In recent years, with the decline in fossil energy and the rise in pollutant emissions, there is an urgent need for efficient and environmentally friendly energy conversion technologies. Supercritical combustion has garnered increasing attention, particularly in the development of advanced engines and gas turbines [1–3]. This process occurs when fuel and oxidizer interact in the supercritical phase, at conditions exceeding their respective critical pressures and temperatures. Owing to the reduced intermolecular distances and accelerated collision dynamics inherent to supercritical fluids, supercritical combustion offers enhanced thermal efficiency and lower pollutant emissions. These advantages make it highly attractive for next-generation internal combustion engines and propulsion systems, including rocket applications [4–6]. A notable example is the Raptor engine used in SpaceX Starship, which operates above 300 atm using a supercritical CH_4/O_2 mixture [7].

At elevated pressures within propulsion systems, fuels undergo local or even global supercritical states, in which the ideal gas assumption fails and intermolecular interactions cannot be neglected. Consequently, it becomes essential to incorporate real-fluid effects,

* Corresponding author.
E-mail address: h.zhao@pku.edu.cn (H. Zhao).

https://doi.org/10.1016/j.combustflame.2025.114465
Received 16 June 2025; Received in revised form 4 September 2025; Accepted 5 September 2025

such as intermolecular interactions and molecular volume, into numerical combustion simulations. Over the past century, a series of semi-empirical real-fluid equations of state, including the van der Waals (VDW) [8], Redlich–Kwong (RK) [9], Soave–Redlich–Kwong (SRK) [10], and Peng–Robinson (PR) [11] models, have been developed to account for real-fluid effects in combustion modeling. For instance, Kogekar [12] employed the RK EoS to investigate the ignition delay times of n-dodecane/O_2/N_2 mixtures under high-pressure conditions. By comparing simulation results with experimental data, it was found that real-fluid effects significantly affect ignition delay times of n-dodecane, particularly in the negative temperature coefficient (NTC) region. Similarly, Liang [13] numerically studied the laminar flame speeds of hydrogen/air and methane/air mixtures under supercritical conditions using the SRK EoS, systematically evaluating the influence of real-fluid effects on combustion characteristics through chemical kinetics, thermodynamics, and transport properties. Li [14–16] also simulated the supercritical oxidation of hydrogen, methane, and ethanol using the PR EoS, further emphasizing the necessity of incorporating real-fluid effects into high-pressure combustion modeling. In addition, Terashima and Koshi [17] developed a real-fluid combustion model and demonstrated that including real-fluid effects significantly improves the prediction accuracy of one-dimensional flame propagation and mass burning rates in H_2/O_2/Ar flames.

While conventional empirical methods for real-fluid modeling are widely used, they exhibit inherent limitations, including dependence on experimental data to fit the parameters of the equation of state (such as a and b in VDW EoS: $P = RT/(\upsilon - b) - a/\upsilon^2$), and a lack of physical insights. To address these shortcomings, Bai et al. [18–20] proposed the LJ-Virial method, which integrates the Lennard-Jones [21] and Stockmayer [22] potentials (collectively referred to as the LJ potential) into the virial equation of state. This approach enables the direct computation of the second and third virial coefficients, as well as Enskog correction factors [23], from LJ potential parameters. These parameters are used to correct the thermodynamic and transport properties of real fluids, thereby eliminating the need for empirical fitting and facilitating real-fluid simulations under supercritical combustion conditions.

However, the LJ-Virial method shows significant limitations at ultra-high pressures, particularly above 200 atm, where it fails to accurately predict the compressibility factors of key species such as CO_2 and H_2O [18]. These deficiencies arise from the oversimplified nature of the LJ potential, which cannot capture the full complexity of intermolecular interactions, especially in systems involving polar molecules, free radicals, and long-chain alkanes that are prevalent in combustion environments [24]. To overcome these critical limitations, our recent work develops the Boltzmann-weighted Full-dimensional (BWF) potential [25]. This model incorporates various interactions and considers the anisotropy and temperature dependence of potential parameters through Boltzmann weighting, providing a more accurate representation of molecular interactions under various conditions. The effectiveness and reliability of this model have been validated through extensive calculations of physical properties and combustion characteristics.

In this study, we integrate the BWF potential into the virial EoS, from which we derive the second and third virial coefficients, and corresponding thermodynamic and transport property expressions of this potential. This method is then integrated into the Cantera software package [26], establishing a new simulation module, the BWF-Virial real-fluid simulation module. Based on this framework, we systematically evaluate thermodynamic and transport properties across nonpolar gases, polar gases, and long-chain alkanes. Furthermore, we employ the BWF-Virial method to simulate zero-dimensional and one-dimensional combustion processes of supercritical methane and n-heptane. These results will provide support for the BWF-Virial approach as a powerful tool for real-fluid combustion modeling under supercritical conditions.

Table 1
List of symbols.

Symbol	Description	Units
p	Pressure	Pa
V	Volume	m^3
υ	Molar volume	m^3/mol
T	Temperature	K
T^*	Dimensionless temperature	–
ρ	Density	kg/m^3
R	Ideal gas constant	J/mol/K
k_B	Boltzmann constant	J/K
$B(T)$	Second virial coefficient	m^3/mol
$C(T)$	Third virial coefficient	m^6/mol^2
$B^*(T^*)$	Dimensionless second virial coefficient	–
$C^*(T^*)$	Dimensionless third virial coefficient	–
ϵ	Potential well depth	J
σ	Molecular diameter	m
r	Intermolecular distance	m
e	Charge	C
μ	Dipole moment	C m
α	Polarizability	C m^2/V
I	First ionization potential	J
L_1	Molecular length	m
L_2	Molecular width	m
η	Viscosity coefficient	μPa s
D	Diffusivity coefficient	cm^2/s
λ	Thermal conductivity	W/m/K
w	Molecular weight	kg/mol
m	Molecular mass	kg
b_0	Gas volume constant	m^3/mol
$\tilde{N}$	Avogadro constant	/mol
$\Omega^{(l,s)*}$	Collision integral	–
$C_{v,\mathrm{rot/trans/vib}}$	The rotational, translational, and vibrational contribution to the molar specific heat of the species	J/mol/K
Z_{rot}	Rotational relaxation collision number	–
y	Correction factor from the partial derivation of the equation of state	–

2. Theory and methods

This section presents the theoretical foundation and computational methodology of the BWF-Virial method. We first introduce the fundamental equations of state and potential models (Section 2.1), followed by detailed derivations of the key physical properties (Section 2.2) and their implementation in the simulation framework (Section 2.3). All the symbols can be found in Table 1.

2.1. Theoretical foundation

2.1.1. Virial equation of state

The ideal gas equation of state provides a good approximation at high temperatures and low pressures:

$$\frac{p\upsilon}{RT} = 1 \tag{1}$$

However, this model deviates significantly from real-fluid behavior near the critical point and in supercritical states. To address this limitation, we employ the virial equation of state, which is derived from statistical mechanics and provides a more accurate description of real-fluid behavior [23]:

$$\frac{p\upsilon}{RT} = 1 + \frac{B(T)}{\upsilon} + \frac{C(T)}{\upsilon^2} \tag{2}$$

where $B(T)$ and $C(T)$ are the second and third virial coefficients, respectively, representing two-body and three-body molecular interactions. The accuracy of this equation depends critically on the accurate determination of these coefficients, which in turn requires a precise description of intermolecular interactions.

2.1.2. Boltzmann-weighted full-dimensional potential model

The accurate representation of intermolecular interactions is crucial for predicting real-fluid behavior. In our previous work [25], we developed the BWF potential model, which provides a comprehensive description of molecular interactions:

$$\begin{aligned}\varphi(r) =&4\varepsilon[(1+2D_s)\left(\frac{\sigma}{r}\right)^{12}+\frac{e^2}{4\varepsilon\sigma}\frac{\sigma}{r}\\&-\left(\frac{2e^2\mu^2}{3k_BT\cdot4\varepsilon\sigma^4}+\frac{\alpha e^2}{4\varepsilon\sigma^4}\right)\left(\frac{\sigma}{r}\right)^4\\&-\left(\frac{2\mu^4}{3k_BT\cdot4\varepsilon\sigma^6}+\frac{2\alpha\mu^2}{4\varepsilon\sigma^6}+\frac{0.75\alpha^2I}{4\varepsilon\sigma^6}\right)\left(\frac{\sigma}{r}\right)^6]\end{aligned} \tag{3}$$

The model incorporates shape effects through the correction factor D_s:

$$D_s = A\left[\left(1-\left(\frac{L_2}{L_1}\right)\right)\right] \tag{4}$$

A is 0.50 for rodlike and −0.25 for platelike molecules. This potential model explicitly accounts for repulsive, induction, dispersion, and electrostatic interactions, while considering the anisotropy and temperature dependence of molecular interactions through Boltzmann weighting.

2.2. Physical properties

2.2.1. Virial coefficients

Based on the BWF potential model, we derive the second and third virial coefficients as shown in Eqs. (5) and (6). The detailed derivation process and interpolation tables are provided in the Supplementary Material:

$$B^*(T^*) = \sum_{n=0}^{\infty} -\frac{2^{\frac{2n+1}{2}}a^n}{4\cdot n!}\Gamma\left(\frac{2n-1}{4}\right)T^{*-\frac{2n+1}{4}} \tag{5}$$

$$\begin{aligned}C^*(T^*) =& \sum_{n=0}^{\infty} -\frac{3}{2}\frac{2^n}{n!}\Gamma\left(\frac{n-1}{2}\right)\\&\int_0^{\frac{3}{4}}\int_{1-\sqrt{1-y^2}}^{\sqrt{1-y^2}} A_n dx d\left(y^2\right)T^{*-\frac{n+1}{2}}\end{aligned} \tag{6}$$

2.2.2. Thermodynamic properties

For multi-component mixtures, we employ a mixture-averaged form of the virial equation of state:

$$p = \frac{RT}{v}\left(1+\frac{B_{\text{mix}}(T)}{v}+\frac{C_{\text{mix}}(T)}{v^2}\right) \tag{7}$$

where the mixture-averaged parameters are calculated as:

$$B_{\text{mix}}(T) = \sum_{i=1}^{m}\sum_{j=1}^{m} B_{ij}(T)x_ix_j \tag{8}$$

$$C_{\text{mix}}(T) = \sum_{i=1}^{m}\sum_{j=1}^{m}\sum_{k=1}^{m} C_{ijk}(T)x_ix_jx_k \tag{9}$$

The total Helmholtz energy for n_T moles of multi-component mixture is:

$$\begin{aligned}A_{\text{mix}} =& \sum_i n_i a_i^0 - \sum_i n_i RT\ln\frac{p^0V}{n_iRT}\\&+ n_TRT\left(\frac{n_TB}{V}+\frac{{n_T}^2C}{2V^2}\right)\end{aligned} \tag{10}$$

The total entropy is:

$$\begin{aligned}S_{\text{mix}} =& \sum_i n_i s_i^0 + n_TR\ln\frac{p^0}{p} - \sum_i n_iR\ln x_i\\&+ n_TR\ln Z\\&- n_TR\left(\frac{n_TB+n_TB_1}{V}+\frac{{n_T}^2C+{n_T}^2C_1}{2V^2}\right)\end{aligned} \tag{11}$$

The total enthalpy is:

$$\begin{aligned}H_{\text{mix}} =& \sum_i n_i h_i^0 - n_TRT + pV\\&- n_TRT\left(\frac{n_TB_1}{V}+\frac{{n_T}^2C_1}{2V^2}\right)\end{aligned} \tag{12}$$

The specific heat capacities at constant pressure and constant volume are calculated as:

$$\begin{aligned}C_p =& \left(\frac{dH}{dT}\right)_{p,n_i}\\=&\left(\frac{dH}{dT}\right)_{V,n_i} - \left[V+T\frac{\left(\frac{dp}{dT}\right)_{V,n_i}}{\left(\frac{dp}{dV}\right)_{T,n_i}}\right]\left(\frac{dp}{dT}\right)_{V,n_i}\end{aligned} \tag{13}$$

$$\begin{aligned}C_v =& \left(\frac{dU}{dT}\right)_{V,n_i}\\=&\left(\frac{dH}{dT}\right)_{V,n_i} - V\left(\frac{dp}{dT}\right)_{V,n_i}\end{aligned} \tag{14}$$

where,

$$\begin{aligned}\left(\frac{dH}{dT}\right)_{V,n_i} =& \sum_i n_i c_{p,i}^0 - n_TR + V\left(\frac{dp}{dT}\right)_{V,n_i}\\&- n_TRT\left(\frac{n_TB_1+n_TB_2}{V}+\frac{{n_T}^2C_1+{n_T}^2C_2}{2V^2}\right)\end{aligned} \tag{15}$$

$$\left(\frac{dp}{dV}\right)_{T,n_i} = -\frac{n_TRT}{V^2}\left(1+\frac{2n_TB}{V}+\frac{3{n_T}^2C}{V^2}\right) \tag{16}$$

$$\left(\frac{dp}{dT}\right)_{V,n_i} = \frac{n_TR}{V}\left(1+\frac{n_TB+n_TB_1}{V}+\frac{{n_T}^2C+{n_T}^2C_1}{V^2}\right) \tag{17}$$

For combustion modeling, we also calculate various partial molar properties. The chemical potential μ_i for species i is:

$$\begin{aligned}\mu_i =&\mu_i^0(T) - RT\ln\frac{p^0}{p} + RT\ln x_i - RT\ln Z\\&+ RT\left(\frac{n_TB+n_TB_i}{V}+\frac{{n_T}^2C+{n_T}^2C_i}{2V^2}\right)\end{aligned} \tag{18}$$

The activity α_i is:

$$\begin{aligned}RT\ln\alpha_i =& - RT\ln\frac{p^0}{p} + RT\ln x_i - RT\ln Z\\&+ RT\left(\frac{n_TB+n_TB_i}{V}+\frac{{n_T}^2C+{n_T}^2C_i}{2V^2}\right)\end{aligned} \tag{19}$$

The partial molar volume is:

$$V_i = \frac{RT\left(1+\frac{n_TB+n_TB_i}{V}+\frac{{n_T}^2C+{n_T}^2C_i}{V^2}\right)}{p+n_TRT\frac{n_TB}{V^2}+n_TRT\frac{2{n_T}^2C}{V^3}} \tag{20}$$

The partial molar enthalpy and entropy are:

$$\begin{aligned}h_i =& \left(\frac{dH}{dn_i}\right)_{V,T,n_j}\\&-\left[V+T\frac{\left(\frac{dp}{dT}\right)_{V,n_i}}{\left(\frac{dp}{dV}\right)_{T,n_i}}\right]\left(\frac{dp}{dn_i}\right)_{V,T,n_j}\end{aligned} \tag{21}$$

$$s_i = \left(\frac{dS}{dn_i}\right)_{V,T,n_j} - \left(\frac{dS}{dp}\right)_{n_i}\left(\frac{dp}{dn_i}\right)_{V,T,n_j} \tag{22}$$

where,

$$\begin{aligned}\left(\frac{dH}{dn_i}\right)_{V,T,n_j} =&h_i^0 - RT + V\left(\frac{dp}{dn_i}\right)_{V,T,n_j}\\&- RT\left(\frac{n_TB_1+n_TB_{i,1}}{V}+\frac{{n_T}^2C_1+{n_T}^2C_{i,1}}{2V^2}\right)\end{aligned} \tag{23}$$

$$\left(\frac{dS}{dn_i}\right)_{V,T,n_j} = s_i^0 + R\ln\frac{p^0 V}{n_i RT} - R - R\left(\frac{n_T B + n_T B_i + n_T B_1 + n_T B_{i,1}}{V}\right) - R\left(\frac{{n_T}^2 C + {n_T}^2 C_i + {n_T}^2 C_1 + {n_T}^2 C_{i,1}}{2V^2}\right) \tag{24}$$

$$\left(\frac{dp}{dn_i}\right)_{V,T,n_j} = \frac{RT}{V}\left(1 + \frac{n_T B + n_T B_i}{V} + \frac{{n_T}^2 C + {n_T}^2 C_i}{V^2}\right) \tag{25}$$

$$\left(\frac{dS}{dp}\right)_{n_i} = \frac{\left(\frac{dp}{dT}\right)_{V,n_i}}{\left(\frac{dp}{dV}\right)_{T,n_i}} \tag{26}$$

The superscript of 0 denotes thermodynamic properties evaluated at atmospheric pressure, while the subscript of i refers to the property of species i. Z represents the compressibility factor, $Z = pV/(n_T RT)$. For the second and third virial coefficients, subscripts "1" and "2" indicate the first and second derivatives with respect to temperature, respectively.

2.2.3. Transport properties

The transport properties are calculated using the kinetic theory of gases, incorporating the BWF potential model. The viscosity coefficient η, mass diffusivity coefficient D, and thermal conductivity coefficient λ are given by [23]:

$$\eta = \frac{5}{16}\frac{\sqrt{\pi m k_B T}}{\pi\sigma^2\Omega^{(2,2)*}} \tag{27}$$

$$D = \frac{3}{16}\frac{\sqrt{\frac{2\pi k_B{}^3 T^3}{m}}}{p\pi\sigma^2\Omega^{(1,1)*}} \tag{28}$$

$$\lambda = \frac{\eta}{w}\left(f_{\text{trans}}C_{v,\text{trans}} + f_{\text{rot}}C_{v,\text{rot}} + f_{\text{vib}}C_{v,vib}\right) \tag{29}$$

In reactive flow simulations, the multicomponent transport model [23] is employed to evaluate species diffusion. The multicomponent diffusion coefficients are calculated using the Stefan–Maxwell equations, which describe the coupled diffusion fluxes of all species in a mixture. To solve these equations efficiently, Chemkin and Cantera employ the L-matrix method. This formulation transforms the Stefan–Maxwell relations into a linear algebra problem, in which the species diffusion velocities are obtained by inverting the L-matrix and multiplying it by a concentration vector. The individual species conductivities are composed of translational, rotational, and vibrational contributions:

$$\begin{aligned} f_{\text{trans}} &= \frac{5}{2}\left(1 - \frac{2}{\pi}\frac{C_{v,\text{rot}}}{C_{v,\text{trans}}}\frac{A}{B}\right), C_{v,\text{trans}} = 1.5R \\ f_{\text{rot}} &= \frac{\rho D}{\eta}\left(1 + \frac{2}{\pi}\frac{A}{B}\right), C_{v,\text{rot,linear}} = 1.0R, C_{v,\text{rot,nonlinear}} = 1.5R \\ f_{vib} &= \frac{\rho D}{\eta}, \quad C_{v,vib} = C_v - C_{v,\text{trans}} - C_{v,\text{rot}} \\ A &= \frac{5}{2} - \frac{\rho D}{\eta}, B = Z_{\text{rot}} + \frac{2}{\pi}\left(\frac{5}{3}\frac{C_{v,\text{rot}}}{R} + \frac{\rho D}{\eta}\right) \end{aligned} \tag{30}$$

To account for pressure effects on transport properties, we employ the Enskog theory correction factors [23]:

$$\frac{\eta v}{\eta^0 b_0} = \frac{1}{y} + 0.8 + 0.761y \tag{31}$$

$$\frac{\lambda v}{\lambda^0 b_0} = \frac{1}{y} + 1.2 + 0.755y \tag{32}$$

$$\frac{pD}{(pD)^0}\frac{v}{b_0} = \frac{1}{y} + 1 \tag{33}$$

$$y = \frac{v}{RT}\left[T\left(\frac{\partial p}{\partial T}\right)_v\right] - 1 \tag{34}$$

where the superscript of 0 indicates transport properties at atmospheric pressure.

2.3. Cantera implementation

The theoretical framework outlined above has been implemented in the Cantera software package. The BWF-Virial module integrates the BWF potential into the virial EoS, enabling the direct calculation of second and third virial coefficients, as well as Enskog correction factors, based solely on the BWF potential parameters. Unlike traditional models that rely heavily on empirical correlations or experimental data fitting, the BWF-Virial module allows for the first-principles prediction of both thermodynamic and transport properties. Consequently, it facilitates high-fidelity simulation of real-fluid behavior and combustion phenomena under a wide range of operating conditions.

3. Results and discussion

3.1. Thermodynamic properties

To evaluate the compressibility factor and thermodynamic properties, including specific enthalpy and isobaric specific heat capacity, we conduct a rigorous comparison of various simulation methods against reference data provided by the National Institute of Standards and Technology (NIST) [27], which is mainly based on experimental data fitting.

Fig. 1 shows the compressibility factor, which characterizes deviations of real-gas behavior from ideality, as a function of pressure for real fluids. At low pressures, all species behave nearly ideally, with compressibility factors close to 1.0. As pressure rises, intermolecular interactions drive significant departures from ideality. For the nonpolar gas H_2, all models, including BWF-Virial, LJ-Virial, RK, and PR, capture the pressure dependence reasonably well. For polar species such as H_2O, RK and PR perform satisfactorily at moderate pressures, but their accuracy deteriorates above 300 atm, with errors exceeding 15%. The LJ-Virial method exhibits even larger deviations, with relative errors surpassing 30%. In contrast, the BWF-Virial method maintains excellent accuracy across the entire range, keeping errors within 5%. For long-chain alkanes such as propane, RK and PR remain reliable at lower pressures, yet deviate from 1% to 7% at higher pressures, while LJ-Virial again shows large discrepancies. The BWF-Virial method consistently performs well, demonstrating its superior capability to represent real-fluid behavior under elevated pressures.

In fuel combustion, the heat release is primarily controlled by the enthalpies of the reactants and products. Fig. 2 shows the pressure dependence of specific enthalpy for various species. For nonpolar gases, such as H_2, all models yield nearly identical predictions, with deviations within 5%. However, for polar species such as H_2O and NH_3, notable discrepancies emerge as pressure increases. The RK and PR methods perform reasonably well, with errors below 10%. The LJ-Virial method shows strong deficiencies, and enthalpies are overestimated by more than 40% (H_2O) and underestimated by more than 80% (NH_3) beyond 300 atm, due to its inadequate treatment of polarity and dense-phase interactions. In contrast, the BWF-Virial method closely follows experimental data across all species and pressure ranges, keeping errors below 10% even under supercritical conditions and for long-chain alkanes.

The isobaric specific heat capacity, a key thermodynamic parameter in isobaric combustion, is shown in Fig. 3 as a function of pressure. As semi-empirical methods fitted by experimental values, the RK and PR methods remain accurate for various species across a wide range of pressures. In contrast, the LJ-Virial method increasingly diverges at elevated pressures, particularly for polar species. For NH_3, its predictions become unstable above 400 atm, sharply overestimating and producing errors up to 270%, reflecting a breakdown of the LJ potential model under supercritical conditions. The BWF-Virial method, however, maintains high fidelity across the entire pressure range, reproducing heat capacities of both nonpolar and polar species with errors below 15% and accurately capturing the gradual increase observed experimentally.

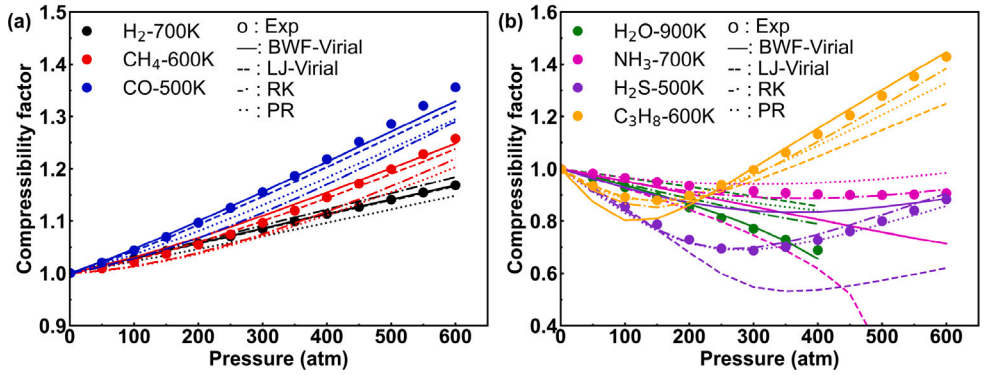

Fig. 1. The compressibility factor computed employing the BWF-Virial, LJ-Virial, RK, and PR methods with comparison to NIST data (a): nonpolar molecules (because of the weak polarity of CO, it is classified to nonpolar species here); (b) polar and long-chain molecules.

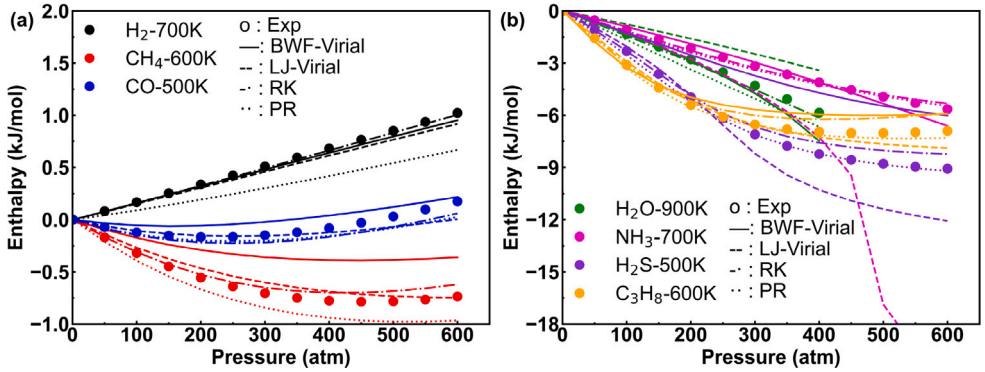

Fig. 2. The specific enthalpy computed employing the BWF-Virial, LJ-Virial, RK, and PR methods with comparison to NIST data (a): nonpolar molecules; (b) polar and long-chain molecules.

3.2. Transport properties

Because of the large experimental measurement uncertainties for diffusion and thermal conductivity, viscosity coefficients provide a reliable method for assessing transport properties [24]. Accordingly, we analyze the viscosity behavior computed by the BWF-Virial, LJ-Virial, and Chung [28] methods, as illustrated in Fig. 4. With increasing pressure, the reduction in intermolecular distances enhances real-fluid interactions, leading to a distinct pressure dependence of viscosity. Utilizing the Enskog theory framework [23], we correct the viscosity coefficients of various species over a wide range of pressures. The BWF-Virial method effectively captures the pressure-induced variations in viscosity, maintaining consistency with expected physical trends. In contrast, the LJ-Virial method performs reasonably well for nonpolar species such as H_2 and CH_4, yet fails to account for the complex interactions in polar molecules like H_2O and NH_3, resulting in pronounced deviations up to 270%. We also provide predictions for diffusion and thermal conductivity coefficients in Figs. S1 and S2 of the Supplementary Material.

Through comprehensive and systematic thermodynamic and transport calculations, the BWF-Virial method demonstrates robust and consistent accuracy across a broad range of pressures. In particular, the method exhibits exceptional predictive capability for polar gases and long-chain alkanes, effectively capturing intricate real-fluid effects that are often inadequately represented by conventional models. These results affirm the BWF-Virial method as a reliable and versatile tool for real-fluid thermodynamic and transport property simulations, offering significant advantages in supercritical modeling.

3.3. Ignition delay time

Building upon the validated reliability of the BWF-Virial method for predicting the thermodynamic and transport properties of real fluids, we conducted an in-depth investigation into the zero-dimensional and one-dimensional combustion characteristics of various fuels. Simulations of ignition delay times and laminar flame speeds were performed in Cantera using the ConstPressureReactor and FreeFlameReactor modules, respectively. Refined computational grids were employed to accurately capture the combustion behavior of supercritical methane and n-heptane. The GRI 3.0 mechanism [29] was utilized for methane, while a reduced n-heptane mechanism [30], derived via path flux analysis (PFA) [31], was used to model long-chain alkane oxidation.

Fig. 5 presents the ignition delay times (IDTs) for methane oxidation in carbon dioxide at 80 atm and 260 atm. A clear temperature dependence is observed, with IDTs decreasing as temperature rises. At 80 atm, all methods, including RK, PR, LJ-Virial, and BWF-Virial, produce similar predictions, slightly underestimating experimental IDTs by 10%–30%. As the pressure increases to 260 atm, significant divergences appear. The RK, PR, and LJ-Virial method overpredicts IDTs by up to 20%–25%. In contrast, the BWF-Virial method captures the pressure-dependent trends most accurately, with predictions approximately 15%–20% lower than LJ-Virial and within 5%–10% of experimental values.

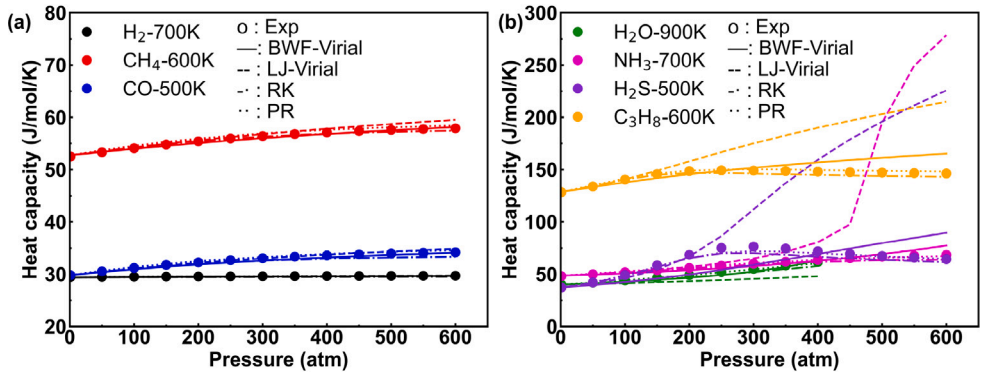

Fig. 3. The isobaric specific heat capacity computed employing the BWF-Virial, LJ-Virial, RK, and PR methods with comparison to NIST data (a): nonpolar molecules; (b) polar and long-chain molecules.

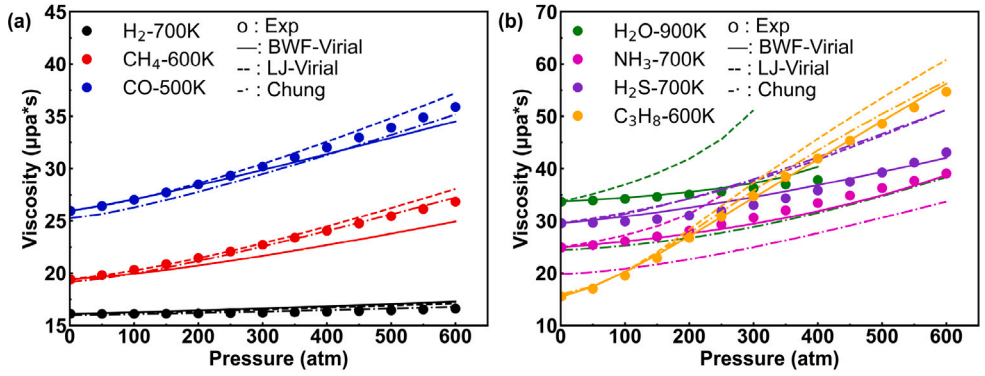

Fig. 4. The viscosity coefficient computed employing the BWF-Virial, LJ-Virial, and Chung methods with comparison to NIST data (a): nonpolar molecules; (b) polar and long-chain molecules.

For n-heptane, ignition delay time simulations at 10 atm and 300 atm are shown in Fig. 6 (RK and PR parameters are difficult to obtain due to the complex composition of the reduced n-heptane mechanism, so Figs. 6 and 8 only show the BWF-Virial, LJ-Virial, and IG models). At 10 atm, both models yield nearly identical results, overestimating the ignition delay time relative to experimental data. However, under the elevated pressure of 300 atm, where molecular spacing is significantly reduced and intermolecular interactions become increasingly pronounced, the predictive performance diverges. In this dense regime, the BWF-Virial method effectively captures the enhancement in ignition reactivity due to intensified collisional dynamics among fuel molecules. As a result, it predicts ignition delay times that are 5%–10% lower than those of the LJ-Virial method.

3.4. Laminar flame speed

Fig. 7 shows the laminar flame speeds of methane/air mixtures at various equivalence ratios under 1 atm and 200 atm. At atmospheric pressure, the Virial and semi-empirical methods yield comparable results, with the BWF-Virial method exhibiting slightly better agreement with experimental data due to its more accurate treatment of transport properties. As the pressure rises to 200 atm, enhanced intermolecular collisions markedly affect flame propagation, amplifying the differences among models. Under these high-pressure conditions, the BWF-Virial method predicts laminar flame speeds up to 20% higher than other approaches, reflecting stronger real-fluid effects on flame dynamics.

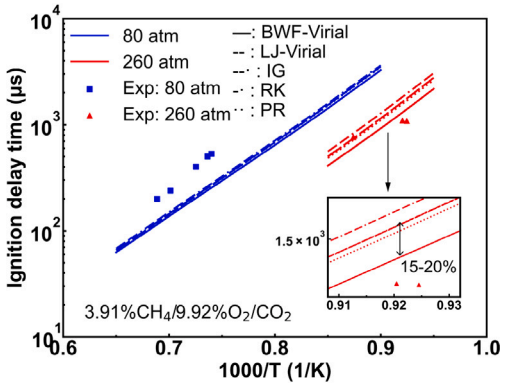

Fig. 5. The ignition delay time modeling for methane oxidation in carbon dioxide with comparison to experimental data [32].

Similarly, Fig. 8 presents the laminar flame speeds of n-heptane/air mixtures. Compared with methane, discrepancies between different methods become more pronounced, even at 1 atm, due to the scarcity of experimental transport data for long-chain hydrocarbons and the heightened sensitivity of laminar flame speed to diffusivity and thermal conductivity. At elevated pressures, the divergence further increases, with the BWF-Virial method predicting flame speeds about 10%–20%

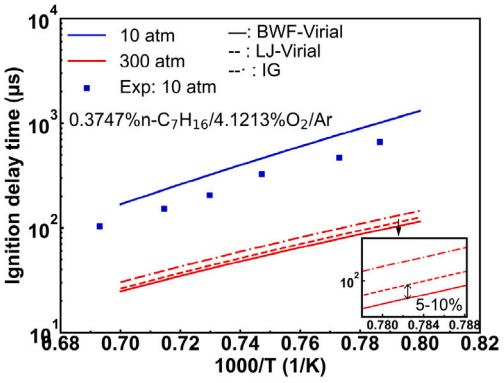

Fig. 6. The ignition delay time modeling for n-heptane oxidation with comparison to experimental data [33].

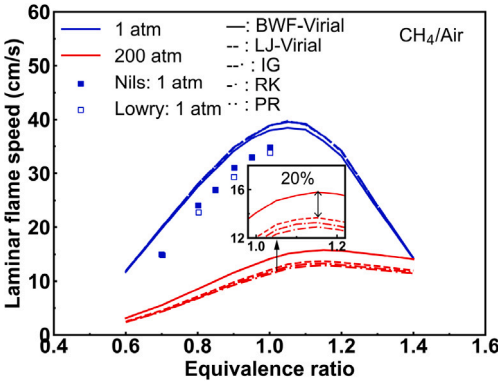

Fig. 7. The laminar flame speed modeling for methane oxidation with comparison to experimental data: Nilsson (Nils) [34], Lowry [35].

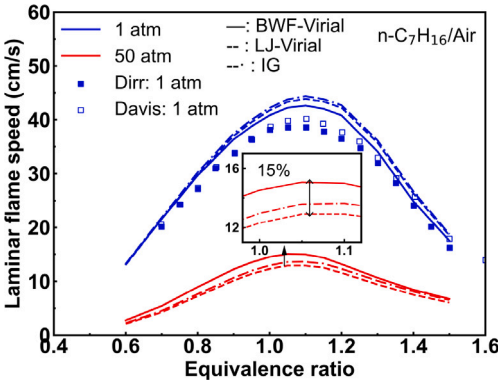

Fig. 8. The laminar flame speed modeling for n-heptane oxidation with comparison to experimental data: Dirrenberger (Dirr) [36], Davis [37].

higher than those from the LJ-Virial method, in closer alignment with experimental trends.

At this stage, our research has yielded significant findings in the areas of compressibility factors, thermodynamic properties, and transport phenomena, as illustrated in Fig. 9. In the future, our work will concentrate on investigating chemical reaction rates from a more microscopic and dynamic perspective, thereby enabling more comprehensive and mechanistically insightful simulations of real-fluid behavior.

4. Conclusion

In this study, we present an extension of the virial equation of state by incorporating the Boltzmann-weighted Full-dimensional potential model. We successfully derive the second and third virial coefficients as well as associated thermodynamic and transport property formulations based on the BWF potential. These theoretical methods are implemented into the Cantera platform, establishing a new simulation module, the BWF-Virial real-fluid method. Unlike conventional empirical methods, the BWF-Virial approach enables real-fluid simulations directly from physically meaningful potential parameters, without reliance on experimental data fitting. Moreover, by incorporating both two-body and three-body molecular interactions based on the BWF potential, the method captures various intermolecular interactions, and the anisotropy and temperature dependence of potential parameters, thereby significantly enhancing the physical accuracy of the virial equation of state.

Extensive simulations of thermodynamic and transport properties across nonpolar gases, polar gases, and long-chain alkanes demonstrate that the BWF-Virial method can maintain a relative error level of 0.1%–10% across a wide range of pressures. Compared with the traditional RK, PR, Chung, and LJ-Virial methods, the BWF-Virial approach reveals superior performance, particularly in modeling real-fluid effects for polar and long-chain molecules. Furthermore, we apply the BWF-Virial method to simulate zero-dimensional ignition delay times and one-dimensional laminar flame speeds for supercritical methane and n-heptane. While both models yield similar results at low pressures, the BWF-Virial method offers significant improvements under elevated and supercritical conditions, with predictions differing by 5%–20% from those of the LJ-Virial method and aligning more closely with experimental data. In the future, we will focus on extending this framework to incorporate microscopic chemical reaction kinetics, further enabling high-fidelity combustion simulations under extreme real-fluid environments.

CRediT authorship contribution statement

Xin Zhang: Writing – original draft, Software, Formal analysis, Conceptualization. **Junfeng Bai:** Validation, Software. **Hao Zhao:** Writing – review & editing, Supervision.

Declaration of competing interest

The authors declare that they have no known competing financial interests or personal relationships that could have appeared to influence the work reported in this paper.

Acknowledgments

This work was supported by the National Natural Science Foundation of China (No. 22350710788, No. 22361132538).

Appendix A. Supplementary data

Supplementary material is submitted along with the manuscript.

Supplementary material related to this article can be found online at https://doi.org/10.1016/j.combustflame.2025.114465.

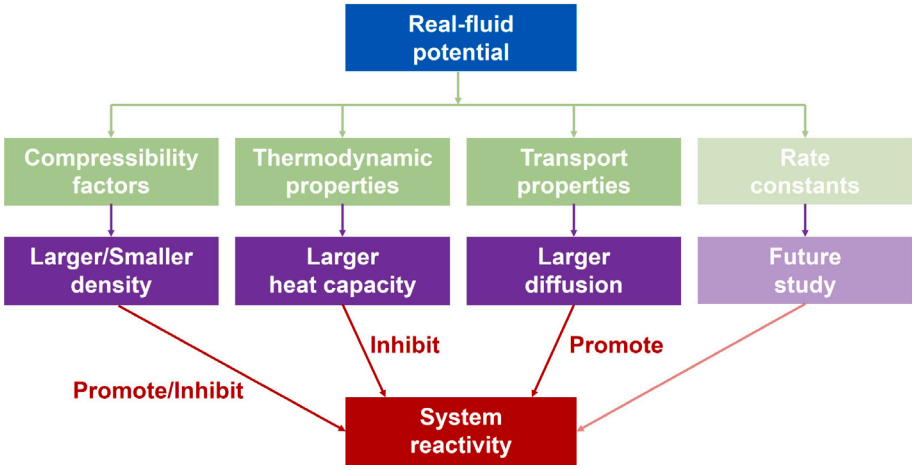

Fig. 9. Diagram of real-fluid effects on reactive flow simulations.

References

[1] G. Lacaze, J.C. Oefelein, A non-premixed combustion model based on flame structure analysis at supercritical pressures, Combust. Flame 159 (2012) 2087–2103.

[2] X. Wang, H. Huo, U. Unnikrishnan, V. Yang, A systematic approach to high-fidelity modeling and efficient simulation of supercritical fluid mixing and combustion, Combust. Flame 195 (2018) 203–215.

[3] P. Gokulakrishnan, J. Shao, M.S. Klassen, D.F. Davidson, R.K. Hanson, NOx formation from ammonia, and its effects on oxy-combustion of hydrocarbon fuels under supercritical-CO2 conditions, Appl. Energy Combust. Sci. 13 (2023) 100110.

[4] H. Zhao, J. Fu, F.M. Haas, Y. Ju, Effect of prompt dissociation of formyl radical on 1,3,5-trioxane and CH2O laminar flame speeds with CO2 dilution at elevated pressure, Combust. Flame 183 (2017) 253–260.

[5] H. Zhao, C. Yan, T. Zhang, G. Ma, M.J. Souza, C.-w. Zhou, Y. Ju, Studies of high-pressure n-butane oxidation with CO2 dilution up to 100 atm using a supercritical-pressure jet-stirred reactor, Proc. Combust. Inst. 38 (2021) 279–287.

[6] P.C. Ma, H. Wu, T. Jaravel, L. Bravo, M. Ihme, Large-eddy simulations of trans-critical injection and auto-ignition using diffuse-interface method and finite-rate chemistry, Proc. Combust. Inst. 37 (2019) 3303–3310.

[7] J.L. Heldmann, M.M. Marinova, D.S.S. Lim, et al., Mission architecture using the SpaceX starship vehicle to enable a sustained human presence on mars, New Space 10 (2022) 259–273.

[8] R.L. Scott, P.H. van Konynenburg, Static properties of solutions. Van der Waals and related models for hydrocarbon mixtures, Discuss. Faraday Soc. 49 (1970) 87–97.

[9] O. Redlich, J.N.S. Kwong, On the thermodynamics of solutions. V. An equation of state. Fugacities of gaseous solutions, Chem. Rev. 44 (1949) 233–244.

[10] G. Soave, Equilibrium constants from a modified Redlich–Kwong equation of state, Chem. Eng. Sci. 27 (1972) 1197–1203.

[11] D.Y. Peng, D.B. Robinson, A new two-constant equation of state, Ind. Eng. Chem. Fund. 15 (1976) 59–64.

[12] G. Kogekar, C. Karakaya, G.J. Liskovich, M.A. Oehlschlaeger, S.C. DeCaluwe, R.J. Kee, Impact of non-ideal behavior on ignition delay and chemical kinetics in high-pressure shock tube reactors, Combust. Flame 189 (2018) 1–11.

[13] W. Liang, W. Li, C.K. Law, Laminar flame propagation in supercritical hydrogen/air and methane/air mixtures, Proc. Combust. Inst. 37 (2019) 1733–1739.

[14] G. Li, Y. Lu, P. Glarborg, Development of a detailed kinetic model for hydrogen oxidation in supercritical H_2O/CO_2 mixtures, Energy Fuels 34 (2020) 15379–15388.

[15] G. Li, Y. Lu, P. Glarborg, Oxidation kinetics of methane and methane/methanol mixtures in supercritical water, Ind. Eng. Chem. Res. 61 (2022) 3889–3899.

[16] G. Li, H. Chen, Y. Zhang, H. Xu, M. Niu, C. Yang, Development of a detailed kinetic model for high-pressure ethanol oxidation in gas phase and supercritical water, J. Supercrit. Fluids 201 (2023) 106025.

[17] H. Terashima, M. Koshi, Prediction of propagating flames under high-pressure conditions with real-fluid combustion modeling, Proc. Combust. Inst. 39 (2023) 1823–1831.

[18] J. Bai, P. Zhang, C.-W. Zhou, H. Zhao, Theoretical studies of real-fluid oxidation of hydrogen under supercritical conditions by using the virial equation of state, Combust. Flame 243 (2022) 111945.

[19] J. Bai, X. Zhang, C.-W. Zhou, P. Zhang, H. Zhao, Theoretical studies of supercritical real-fluid oxidations of diverse fuels by using the 3rd-order virial equation of state with nonlinear effects, Combust. Flame 270 (2024) 113728.

[20] J. Bai, X. Zhang, H. Zhao, Theoretical study of the real-fluid laminar flame propagation under supercritical conditions by using the virial equation of state and the Enskog transport model, Combust. Flame 276 (2025) 114144.

[21] J.E. Lennard-Jones, On the determination of molecular fields. —II. From the equation of state of a gas, Proc. R. Soc. Lond. A 106 (1924) 463–477.

[22] W.H. Stockmayer, Second virial coefficients of polar gases, J. Chem. Phys. 9 (1941) 398–402.

[23] J.O. Hirschfelder, C.F. Curtiss, R.B. Bird, Molecular Theory of Gases and Liquids, second ed., John Wiley and Sons, Inc., New York, NY, 1964.

[24] N.J. Brown, L.A.J. Bastien, P.N. Price, Transport properties for combustion modeling, Prog. Energy Combust. Sci. 37 (2011) 565–582.

[25] X. Zhang, J. Bai, B. Liu, T. Zhu, H. Zhao, Real-fluid transport property computations based on the Boltzmann-weighted full-dimensional potential model, Appl. Energy Combust. Sci. 23 (2025) 100342.

[26] D.G. Goodwin, H.K. Moffat, I. Schoegl, R.L. Speth, B.W. Weber, Cantera: An object-oriented software toolkit for chemical kinetics and thermodynamics and and transport processes, 2023, http://dx.doi.org/10.5281/zenodo.8137090, Version 3.0.0. https://www.cantera.org.

[27] M. Chase, C. Davies, J. Downey, D. Frurip, R. McDonald, A. Syverud, NIST JANAF thermochemical tables, 1985, Version 1.0. https://webbook.nist.gov/chemistry/.

[28] T.-H. Chung, M. Ajlan, L.L. Lee, K.E. Starling, Generalized multiparameter correlation for nonpolar and polar fluid transport properties, Ind. Eng. Chem. Res. 27 (1988) 671–679.

[29] P. Smith, D.M. Golden, M. Frenklach, et al., GRI-mech 3.0, 2000, Version 3.0. http://combustion.berkeley.edu/gri-mech/.

[30] H.J. Curran, P. Gaffuri, W.J. Pitz, C.K. Westbrook, A comprehensive modeling study of iso-octane oxidation, Combust. Flame 129 (2002) 253–280.

[31] W. Sun, Z. Chen, X. Gou, Y. Ju, A path flux analysis method for the reduction of detailed chemical kinetic mechanisms, Combust. Flame 157 (2010) 1298–1307.

[32] J. Shao, R. Choudhary, D.F. Davidson, R.K. Hanson, S. Barak, S. Vasu, Ignition delay times of methane and hydrogen highly diluted in carbon dioxide at high pressures up to 300 Atm, Proc. Combust. Inst. 37 (2019) 4555–4562.

[33] J. Zhang, S. Niu, Y. Zhang, C. Tang, X. Jiang, E. Hu, Z. Huang, Experimental and modeling study of the auto-ignition of n-heptane/n-butanol mixtures, Combust. Flame 160 (2013) 31–39.

[34] E.J.K. Nilsson, A. van Sprang, J. Larfeldt, A.A. Konnov, The comparative and combined effects of hydrogen addition on the laminar burning velocities of methane and its blends with ethane and propane, Fuel 189 (2017) 369–376.

[35] W. Lowry, J. de Vries, M. Krejci, et al., Laminar flame speed measurements and modeling of pure alkanes and alkane blends at elevated pressures, J. Eng. Gas Turbines Power 133 (2011) 091501.

[36] P. Dirrenberger, P.A. Glaude, R. Bounaceur, H.L. Gall, A.P. da Cruz, A.A. Konnov, F.B. Leclerc, Laminar burning velocity of gasolines with addition of ethanol, Fuel 115 (2014) 162–169.

[37] S.G. Davis, C.K. Law, Determination of and fuel structure effects on laminar flame speeds of C_1 to C_8 hydrocarbons, Combust. Sci. Technol. 140 (1998) 427–449.